
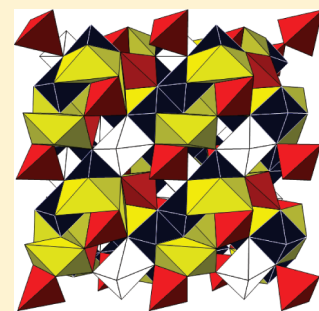


Lithium-Ion Conduction Pathways in Complex Lithium Spinel $\text{Li}_2\text{MGe}_3\text{O}_8$ (M = Ni or Zn)

Nik Reeves-McLaren,^{*,†} Ronald I. Smith,[‡] and Anthony R. West[†][†]Department of Materials Science and Engineering, University of Sheffield, Sheffield S1 3JD, U.K.[‡]ISIS Facility, Science and Technology Facilities Council, Rutherford Appleton Laboratory, Harwell Oxford, Didcot, Oxfordshire OX11 0QX, U.K. Supporting Information

ABSTRACT: Crystal structures of $\text{Li}_2\text{MGe}_3\text{O}_8$ (M = Ni or Zn), in space group $P4_332$, have been refined by application of the Rietveld method to variable-temperature time-of-flight neutron powder diffraction data. Difference Fourier maps, calculated using data collected at high temperatures, showed significant negative density centered at positions vacant at ambient temperatures. In $\text{Li}_2\text{NiGe}_3\text{O}_8$, conduction involves three-dimensional 8c–12d–8c site hopping, facilitated by harmonic oscillations of oxygen atoms away from their ideal positions. For $\text{Li}_2\text{ZnGe}_3\text{O}_8$, the pathway involves a more complex 4b–24e–4a–24e–4b mechanism.

KEYWORDS: spinels, conduction pathways, solid electrolyte, lithium-ion battery materials



INTRODUCTION

Research on new lithium-ion conducting electrolyte materials for use in rechargeable lithium batteries has been significant in recent years. Solid electrolytes have a number of advantages over liquid electrolytes, e.g. simpler and safer cell design, resistance to changes in conditions (e.g. shock–vibration or temperature–pressure), and electrochemical stability.¹ Electrochemical instability in contact with liquid electrolytes has been particularly problematic in the development of high-voltage Li-ion battery cathode materials; more stable electrolytes would open the field of materials operating at or above 5 V, e.g. LiCoMnO_4 ,² for further development.

The largest issue facing development of improved solid electrolytes is their ionic conductivity: for commercialization, ambient-temperature conductivities, σ , of at least 10^{-3} S/cm must be achieved. The best crystalline materials in the field include the perovskite-structured $\text{La}_{0.5}\text{Li}_{0.5}\text{TiO}_3$ ($\sigma = 1 \times 10^{-3}$ S/cm at 300 K^{3-5}) and garnet phases such as $\text{Li}_6\text{BaLa}_2\text{Ta}_2\text{O}_{12}$ ($\sigma = 5 \times 10^{-3}$ S/cm at 300 K^{6-10}), though all materials studied to date have significant issues that prevent their application in commercial cells.¹¹

The mechanisms for Li^+ -ion conduction in these materials are often poorly understood, with only a limited number of studies having been published in this area; an improved understanding of the processes involved may be key to the development of new materials with higher ionic conductivity. Experiments by Várez et al.¹² on $\text{Li}_{3x}\text{La}_{2/3-x}\text{TiO}_3$ used difference Fourier maps calculated from neutron diffraction data to show that at high temperatures Li cations became disordered over a number of crystallographic sites in the perovskite structure; Yashima¹³ used a maximum entropy method to fit neutron diffraction data and show a 2c–4f–2c migration pathway through La-deficient layers

in $\text{Li}_{0.16}\text{La}_{0.62}\text{TiO}_3$. Ishizawa et al.^{14,15} used a combination of synchrotron X-ray diffraction and molecular dynamics simulation to investigate Li-ion conduction pathways in LiMn_2O_4 and showed that not all Li atoms were located on the ideal 8a site of the $Fd\bar{3}m$ spinel structure but instead were partially distributed along the 8a–16c tie line; the mechanism also involved a statistical distribution of O atoms around their ideal 32e positions, possibly related to local Jahn–Teller distortions, which effectively opened the bottleneck in the tetrahedral face to permit Li-ion hopping. This is supported by the recent findings of Laumann et al.¹⁶ for spinel $\text{Li}_4\text{Ti}_5\text{O}_{12}$, where Rietveld refinement using neutron powder diffraction data showed Li on split 32e sites rather than exactly on 16c, resulting in an 8a–32e–32e–8a pathway.

The spinel structure, general formula AB_2O_4 , was independently reported by Bragg¹⁷ and Nishikawa.¹⁸ Spinel is generally described in terms of the arrangements of cations over the tetrahedral and octahedral interstices in a near-ideal cubic close packed (ccp) array of oxide anions, i.e., whether normal ($[\text{A}]^{\text{tet}}[\text{B}_2]^{\text{oct}}\text{O}_4$), inverse ($[\text{B}]^{\text{tet}}[\text{A},\text{B}]^{\text{oct}}\text{O}_4$), or random ($[\text{B}_{0.67}\text{A}_{0.33}]^{\text{tet}}[\text{A}_{0.67}\text{B}_{1.33}]^{\text{oct}}\text{O}_4$). With eight AB_2O_4 formula units per unit cell,¹⁹ 96 interstices are created, of which only 24 (8 of 64 possible tetrahedral and 16 of 32 octahedral interstices) are occupied by cations, offering intriguing possibilities for three-dimensional conduction pathways, where ions can migrate in a relatively unobstructed manner through the crystal structure. The structure may be envisaged as a three-dimensional network of edge-sharing BO_6 octahedra, which share corners with AO_4 tetrahedra.

Received: May 20, 2011

Revised: June 17, 2011

Published: July 12, 2011

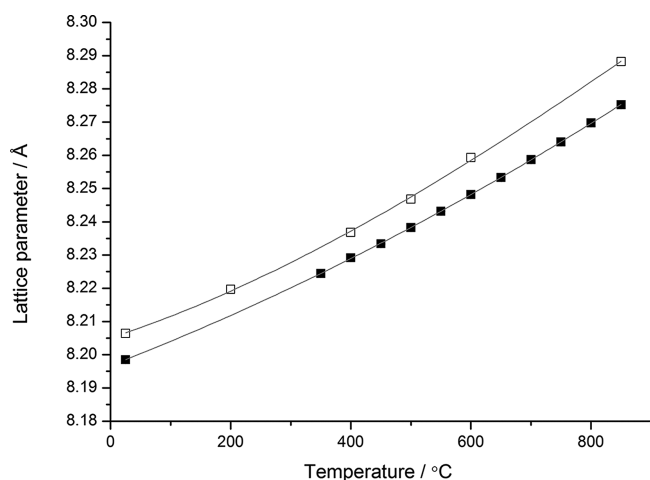


Figure 1. Lattice parameters of $\text{Li}_2\text{NiGe}_3\text{O}_8$ (■) and $\text{Li}_2\text{ZnGe}_3\text{O}_8$ (□) as a function of temperature, from neutron powder diffraction data. Estimated standard deviations are smaller than the symbols.

The aim of this work is to investigate the Li^+ -ion conduction pathway in ordered ternary spinel compounds, $[\text{A}_{2-i}\text{B}_i]_{\text{tet}}[\text{A}_i\text{B}_{1-i}]_{\text{oct1}}[\text{B}'_3]_{\text{oct2}}\text{O}_8$, where i is the degree of inversion.^{20–22} $\text{Li}_2\text{NiGe}_3\text{O}_8$ was previously reported by Kawai et al.^{23,24} to exhibit modest Li^+ -ion conductivity of $\sim 1 \times 10^{-5}$ S/cm at 63 °C. Its structure can be described as a fully ordered normal cubic spinel, with Li^+ ions occupying a tetrahedral 8c site and 1:3 cation ordering of Ni and Ge over 4b and 12d octahedral sites, respectively, in the $P4_332$ space group, an ordered subgroup of the ideal $Fd\bar{3}m$ spinel space group. $\text{Li}_2\text{NiGe}_3\text{O}_8$ does not undergo any phase transitions upon heating, and there is no evidence of cation mixing across tetrahedral or octahedral sites. It was therefore an ideal candidate material in which to identify the Li^+ -ion conduction mechanism by analysis of difference Fourier maps obtained from Rietveld refinement of structural models using variable-temperature neutron powder diffraction experiments. The findings are compared with those for a fully inverse ordered ternary spinel, $\text{Li}_2\text{ZnGe}_3\text{O}_8$, which exhibits²⁴ extremely low ionic conductivity. In $\text{Li}_2\text{ZnGe}_3\text{O}_8$, the 8c site is filled by Li and Zn, with the remaining Li on the octahedral 4b site.

EXPERIMENTAL SECTION

Li_2CO_3 (dried at 180 °C; natural isotopic abundance of Li), NiO, ZnO, and GeO_2 (dried at 500 °C) were used as reagents. Appropriate amounts of each reagent were mixed in an agate mortar and pestle, then placed in Au foil boats, and fired at 650 °C for 5 h, for decarbonation of the lithium reagent, and then at 800 °C for 45 h, with intermittent regrinding, to complete the reaction.

X-ray powder diffraction (XRD) used a STOE STADI P diffractometer, $\text{Cu K}\alpha_1$ radiation ($\lambda = 1.54056$ Å), and an image plate detector for phase analysis. Initial data analysis used STOE's WinX^{POW}.

Variable-temperature time-of-flight (ToF) neutron powder diffraction (ND) data were collected on the POLARIS powder diffractometer at the ISIS Facility, Rutherford Appleton Laboratory. The sample was placed in a vanadium can and mounted within an evacuated high-temperature furnace; data were collected for ~ 2 h and corrected for absorption. Diffraction patterns were collected over the range of 25–850 °C. Rietveld refinement used the EXPGUI²⁵ interface for GSAS²⁶ on data collected in the backscattering detector bank (0.2 Å $\leq d \leq 3.2$ Å; resolution $\Delta d/d \sim 5 \times 10^{-3}$); the errors quoted are as given by GSAS.

Table 1. Refined Structure Parameters and Derived Bond Lengths for $\text{Li}_2\text{NiGe}_3\text{O}_8$ at Room Temperature

space group	$P4_332$
a (Å)	8.19851 (10)
V (Å ³)	551.07 (2)
χ^2	2.343
R_{wp} (%)	2.36
R_{p} (%)	3.77
cation site 8c	
x ($= y = z$)	0.00404 (55)
site occupancy	1.0 Li
U_{iso} (Å ²)	0.0118 (4)
cation site 4b	
x ($= y = z$)	0.625
site occupancy	1.0 Ni
U_{iso} (Å ²)	0.0035 (2)
cation site 12d	
x	0.125
y	0.37774 (8)
z	0.87227 (8)
site occupancy	1.0 Ge
U_{iso} (Å ²)	0.0022 (1)
oxygen site 1, O1, 8c	
x ($= y = z$)	0.38454 (10)
site occupancy	1.0 O
U_{iso} (Å ²)	0.0033 (2)
oxygen site 2, O2, 24e	
x	0.10016 (12)
y	0.12643 (10)
z	0.39408 (12)
site occupancy	1.0 O
U_{iso} (Å ²)	0.0035 (1)
bond length (Å)	
Li–O1	1.968 (8) \times 1
Li–O2	1.9657 (23) \times 3
Ni–O2	2.0773 (8) \times 6
Ge–O1	1.9531 (10) \times 2
Ge–O2	1.8732 (12) \times 2, 1.9019 (11) \times 2

RESULTS

Phase pure samples of $\text{Li}_2\text{NiGe}_3\text{O}_8$ and $\text{Li}_2\text{ZnGe}_3\text{O}_8$ were obtained. XRD data were indexed on the $P4_332$ space group, with no additional or missing reflections. When the samples were heated to 850 °C, analysis of neutron powder diffraction data showed the samples remained single phase, with an increase in lattice parameters deviating slightly away from linearity (Figure 1).

Rietveld Refinement of the $\text{Li}_2\text{NiGe}_3\text{O}_8$ Crystal Structure at 25 °C. Using the ambient-temperature crystal structure of $\text{Li}_2\text{NiGe}_3\text{O}_8$ previously reported from XRD data,²⁴ the initial structural model had Li on the tetrahedral 8c site, Ni and Ge on 4b and 12d octahedral sites, respectively, and oxygen on 8c and 24e sites. Total occupancies for all sites were fixed to unity with initial isotropic thermal displacement parameters, U_{iso} , of 0.005 Å².

The background and scale factors were refined first, using a shifted Chebyshev function with six terms for the background, followed by the lattice and profile parameters. Atomic positions were refined in order of decreasing scattering length magnitude,

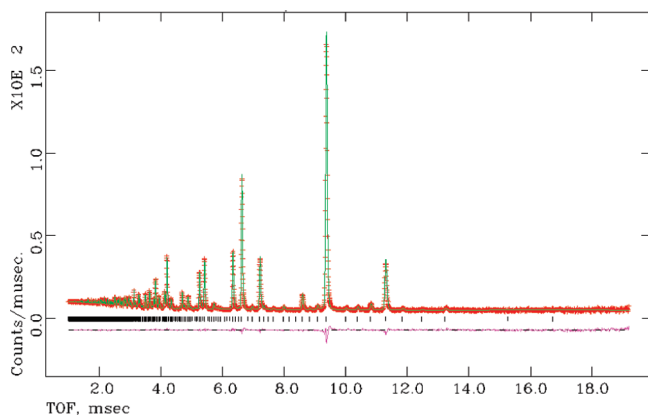


Figure 2. Observed, calculated, and difference profiles from ToF ND data for $\text{Li}_2\text{NiGe}_3\text{O}_8$ at room temperature.

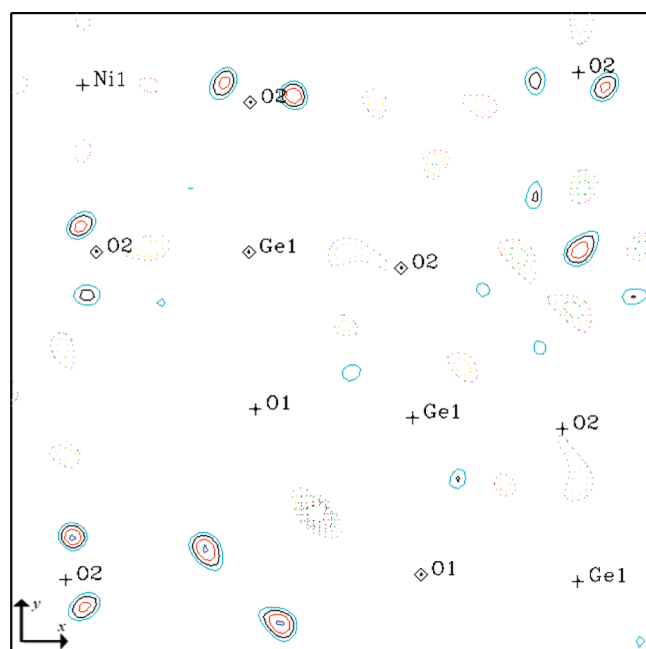


Figure 3. Difference Fourier map for the $z = 0.375$ section (map size of $8 \text{ \AA} \times 8 \text{ \AA}$) calculated during Rietveld refinement of the $\text{Li}_2\text{NiGe}_3\text{O}_8$ crystal structure at $850 \text{ }^\circ\text{C}$. The negative scattering well, later attributed to Li on a distorted 12d octahedral site, is located between O1 atoms. Solid and dashed contours refer to positive and negative scattering density, respectively.

followed by U_{iso} values, and finally the diffractometer constant, DIFA. The whole process was repeated until convergence, with negligible shifts in atomic variables, was achieved.

The statistical measures (Table 1) and a visual fit of the data (Figure 2) were relatively good ($\chi^2 = 2.343$, and discrepancy, or R_f factors of $<4\%$). Refined U_{iso} values for Ni, Ge, and O were all acceptably low.

Rietveld Refinement of the $\text{Li}_2\text{NiGe}_3\text{O}_8$ Crystal Structure at $850 \text{ }^\circ\text{C}$. Rietveld refinement on ToF ND data collected for $\text{Li}_2\text{NiGe}_3\text{O}_8$ at $850 \text{ }^\circ\text{C}$ used the same initial model and refinement strategy. It should be noted that, strictly, initial U_{iso} values of 0.005 \AA^2 are too small for a data set collected at such high temperatures; larger and anisotropic initial thermal displacement

Table 2. Refined Structure Parameters and Derived Bond Lengths for $\text{Li}_2\text{NiGe}_3\text{O}_8$ at $850 \text{ }^\circ\text{C}$

space group	$P4_332$
a (\AA)	8.27527 (15)
V (\AA^3)	566.69 (3)
χ^2	2.254
R_{wp} (%)	2.51
R_p (%)	3.77
refined stoichiometry	$\text{Li}_{2.03(7)}\text{NiGe}_3\text{O}_8$
cation site 8c	
x ($= y = z$)	0.01895 (38)
site occupancy	0.860 (14) Li
U_{iso} (\AA^2)	0.005
cation site 12d	
x	-0.2310 (43)
y	0.875
z	0.0190 (43)
site occupancy	0.104 (16) Li
U_{iso} (\AA^2)	0.005
cation site 4b	
x ($= y = z$)	0.625
site occupancy	1.0 Ni
U_{iso} (\AA^2)	0.0140 (6)
cation site 12d	
x	0.125
y	0.37826 (15)
z	0.87175 (15)
site occupancy	1.0 Ge
U_{iso} (\AA^2)	0.0099 (2)
oxygen site 1, O1, 8c	
x ($= y = z$)	0.38524 (20)
site occupancy	1.0 O
U_{ij} (\AA^2)	0.0136 (7) $\times 3$, -0.0043 (10)
oxygen site 2, O2, 24e	
x	0.09857 (22)
y	0.12678 (21)
z	0.39480 (20)
site occupancy	1.0 O
U_{ij} (\AA^2)	0.0118 (8), 0.0227 (8), 0.0063 (8), 0.0036 (7), -0.0056 (5), 0.0016 (9)
bond length (\AA)	
$\text{Li}_{8c}\text{-O1}$	2.210 (6) $\times 1$
$\text{Li}_{8c}\text{-O2}$	1.9422 (16) $\times 3$
$\text{Li}_{12d}\text{-O1}$	1.505 (11) $\times 2$
$\text{Li}_{12d}\text{-O2}$	2.444 (26) $\times 2$, 2.450 (31) $\times 2$
Ni-O2	2.0970 (20) $\times 6$
Ge-O1	1.9621 (17) $\times 2$
Ge-O2	1.8762 (20) $\times 2$, 1.9259 (17) $\times 2$

parameters for Li sites would have been more appropriate. However, this approach resulted in attribution of the density resulting from Li-ion diffusion simply to enlarged thermal ellipsoids. Use of small isotropic thermal parameters permitted identification of intermediate sites in the Li-ion conduction pathway.

This initial model gave good visual fit and statistical measures (Table 1 of the Supporting Information), although the U_{iso} for Li was quite large, 0.0417 (13) \AA^2 . Resetting this to the fixed initial

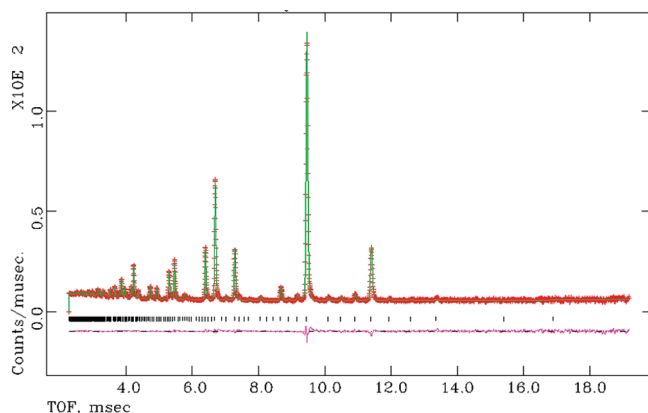


Figure 4. Observed, calculated, and difference profiles from ToF ND data for $\text{Li}_2\text{NiGe}_3\text{O}_8$ at 850°C , using the structural model described in Table 3, with Li distributed over two crystallographic sites.

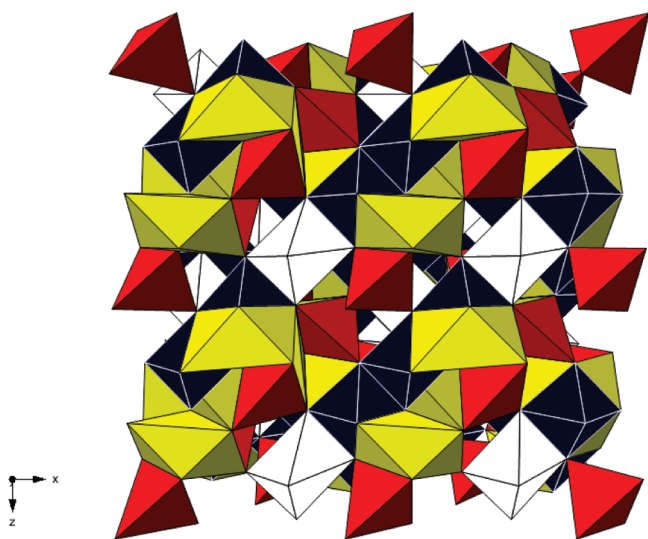


Figure 5. Refined spinel structure of $\text{Li}_2\text{NiGe}_3\text{O}_8$ at 850°C , showing white NiO_6 , dark blue GeO_6 octahedra, red $\text{Li}_{8c}\text{-O}_4$ tetrahedra, and yellow $\text{Li}_{12d}\text{-O}_6$ octahedra.

value, 0.005 \AA^2 , gave a refined Li_{8c} occupancy of 0.860 (14). Difference Fourier maps at this stage showed significant negative density at approximately $-0.23, 0.875, 0.018$ and equivalent positions (Figure 3). As the scattering lengths for Ni, Ge, and O are all positive (10.3, 8.19, and 5.80 fm, respectively), this extra scattering can be attributed to only Li (scattering length of -1.90 fm).

Refinement was continued with a second crystallographically distinct lithium site added to the structure at the 12d position at $-0.23, 0.875$, and 0.018 . Because of possible correlations between site occupancy and thermal displacement parameters, the U_{iso} values for Li_{8c} and Li_{12d} sites were fixed at the initial values. Thermal parameters for Ni, Ge, and O sites were refined together with fractional occupancies of both Li_{8c} and Li_{12d} sites, without constraints.

The Li_{12d} octahedral site is coordinated by O1 and O2 atoms and is heavily distorted, with Li displaced by $\sim 0.17 \text{ \AA}$ from the centroid position. $\text{Li}_{12d}\text{-O}_6$ octahedra share two edges with nearest neighbor $\text{Li}_{8c}\text{-O}_4$ tetrahedra; each $\text{Li}_{8c}\text{-O}_4$ tetrahedron

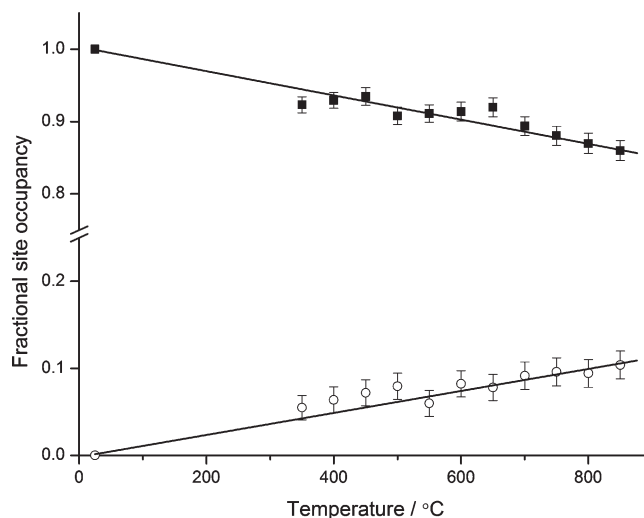


Figure 6. Refined fractional occupancy of Li on 8c (■) and 12d (○) sites in $\text{Li}_2\text{NiGe}_3\text{O}_8$ as a function of temperature.

is surrounded by three $\text{Li}_{12d}\text{-O}_6$ octahedra with interatomic $\text{Li}_{8c}\text{-Li}_{12d}$ distances of 2.361 (22) \AA . The $\text{Li}_{12d}\text{-O}_1$ distance (Table 2) is unfeasibly short, $\sim 1.50 \text{ \AA}$, while $\text{Li}_{12d}\text{-O}_2$ distances are rather long. Difference Fourier maps (Figure 3) show significant extra nuclear density spread around the ideal position of the O2 atom. It appears, therefore, that occupation of the Li_{12d} site induces local structural distortions, shifting oxygen atoms from their ideal position, in a manner similar to that reported for Li-ion conduction in LiMn_2O_4 by Ishizawa et al.,^{14,15} with resulting distortions of adjacent GeO_6 and/or NiO_6 octahedra. Refining anisotropic thermal displacement parameters for O1 and O2 resulted in enlarged, flattened thermal ellipsoids and a significantly improved fit (Figure 4).

The results for this final structural model are presented in Table 2 and Figure 5. The Li_{8c} site was $\sim 86\%$ occupied, with the new 12d site $\sim 10\%$ occupied, giving a total Li content in good agreement with that expected, to within one estimated standard deviation (esd). There was no evidence of any long-range ordering over the two Li sites.

Variation in Li Site Occupancies in $\text{Li}_2\text{NiGe}_3\text{O}_8$ with Temperature. This new structural model was refined using ToF ND data collected at various temperatures from 350 to 800°C . Refined 8c site occupancies decreased linearly, while site 12d occupancies increased linearly, as a function of temperature (Figure 6). The total lithium content always remained close to 2, within one esd (Figure 7).

Cation–oxygen bond lengths are summarized in Figure 8. Ni–O2 bonds were lengthened slightly with temperature, while all Ge–O and $\text{Li}_{8c}\text{-O}_2$ bond lengths remained constant, within esds. However, the $\text{Li}_{8c}\text{-O}_1$ bond length increased significantly, reaching 2.185 (6) \AA at 850°C ; O1–O2 and O2–O2 distances around the Li_{8c} tetrahedral site also increased. These results show that, as the temperature increases, there is a concomitant enlargement of the tetrahedral faces around Li_{8c} sites.

Rietveld Refinement of the $\text{Li}_2\text{ZnGe}_3\text{O}_8$ Crystal Structure at 25 and 850°C . The starting model for refinements of the crystal structure of $\text{Li}_2\text{ZnGe}_3\text{O}_8$ again came from Kawai et al.²⁴ $\text{Li}_2\text{ZnGe}_3\text{O}_8$ is an inverse spinel; the 8c site is shared by Li and Zn and the octahedral 4b site occupied solely by Li. Total occupancies were fixed to unity, and initial U_{iso} values were 0.005 \AA^2 .

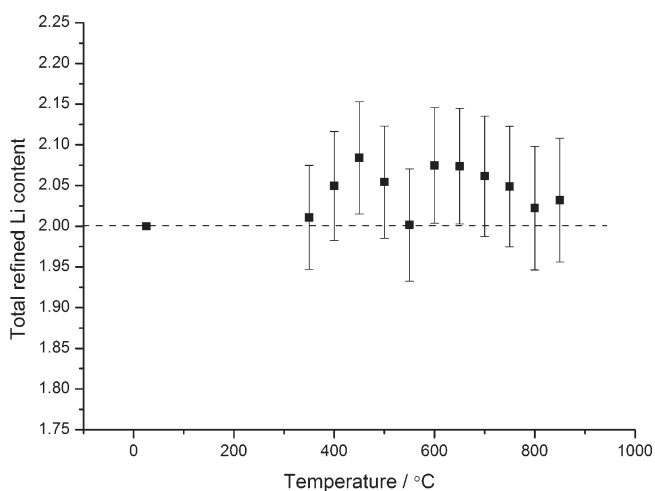


Figure 7. Refined total Li content of $\text{Li}_2\text{NiGe}_3\text{O}_8$ as a function of temperature.

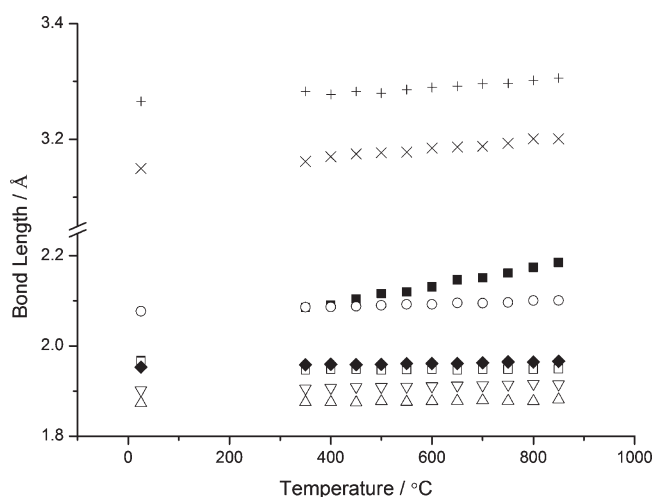


Figure 8. Variation with temperature of $\text{Li}_{8c}\text{-O1}$ (■), $\text{Li}_{8c}\text{-O2}$ (□), Ni-O2 (○), Ge-O1 (◆), and Ge-O2 (hourglass) bond lengths in $\text{Li}_2\text{NiGe}_3\text{O}_8$. O1-O2 (×) and O2-O2 (+) distances around the Li_{8c} site are also shown. Estimated standard deviations are smaller than the symbols.

Refinements using ambient-temperature data followed the strategy outlined for $\text{Li}_2\text{NiGe}_3\text{O}_8$, with results presented in Table 3; a good fit was obtained (Figure 9), with acceptable statistical measures. Refined U_{iso} values were acceptable for all positions; while the value for the 4b site is a little higher than others, it was not high enough to suggest a serious issue with this site. Bond lengths (Table 3) show a slight increase in the degree of distortion of the 8c and 12d polyhedra in comparison with $\text{Li}_2\text{NiGe}_3\text{O}_8$.

The results at 850 °C using the initial structural model are presented in Table 2 of the Supporting Information; while the fit and statistical measures ($\chi^2 = 2.042$; $R_{\text{wp}} = 2.50\%$; $R_{\text{p}} = 3.81\%$) were good, the U_{iso} for the 4b site was unacceptably large, 0.0786 (52) \AA^2 . Resetting this to the initial value of 0.005 \AA^2 and allowing the Li occupancy to vary yielded a significant reduction in Li content, to 0.596 (21). Difference Fourier maps showed significant negative density, which can be attributed to Li, on a

Table 3. Refined Structure Parameters and Derived Bond Lengths for $\text{Li}_2\text{ZnGe}_3\text{O}_8$ at Room Temperature

space group	$P4_332$
a (Å)	8.20638 (10)
V (Å ³)	552.656 (21)
χ^2	1.655
R_{wp} (%)	2.22
R_{p} (%)	3.64
cation site 8c	
x ($= y = z$)	0.00405 (25)
site occupancy	0.5 Li/0.5 Zn
U_{iso} (Å ²)	0.0009 (3)
cation site 4b	
x ($= y = z$)	0.625
site occupancy	1.0 Li
U_{iso} (Å ²)	0.0170 (13)
cation site 12d	
x	0.125
y	0.37465 (7)
z	0.87535 (7)
site occupancy	1.0 Ge
U_{iso} (Å ²)	0.0031 (1)
oxygen site 1, O1, 8c	
x ($= y = z$)	0.38688 (9)
site occupancy	1.0 O
U_{iso} (Å ²)	0.0030 (2)
oxygen site 2, O2, 24e	
x	0.09921 (8)
y	0.13139 (9)
z	0.39453 (7)
site occupancy	1.0 O
U_{iso} (Å ²)	0.0036 (1)
bond length (Å)	
$\text{Li}/\text{Zn}_{8c}\text{-O1}$	2.003 (4) \times 1
$\text{Li}/\text{Zn}_{8c}\text{-O2}$	1.9547 (11) \times 3
$\text{Li}_{4b}\text{-O2}$	2.1207 (8) \times 6
Ge-O1	1.9617 (10) \times 2
Ge-O2	1.8450 (10) \times 2, 1.9042 (6) \times 2

vacant 4a octahedral site at 0.125, 0.125, 0.125 and equivalent positions. Refinement of a revised structural model, with Li distributed over 8c, 4b, and 4a sites, gave a total Li content of only ~ 1.73 . Difference Fourier maps were again calculated to locate the remaining Li and a possible site, 24e, identified at $\sim 0.98, 0.18, 0.01$. This site lies between the 8c tetrahedra and the faces of the $4b\text{-O}_6$ octahedra nearest to the 4a site.

A revised structural model, with Li now distributed over four sites, was refined. The occupancy of the 8c site was fixed at 0.5 Li/0.5 Zn because its thermal displacement parameter was acceptable, difference Fourier maps did not indicate any issues, and, even when the occupancy was allowed to vary, it did not change significantly. U_{iso} values for 4b, 4a, and 24e sites were fixed at default values; U_{iso} values for Ni, Ge, and O sites were refined together with fractional occupancies for 4b, 4a, and 24e Li sites, without constraints. A good fit was obtained (Figure 10).

All refined U_{iso} values and fractional site occupancies (Table 4) now gave acceptable values, and the refined Li site occupancies give an overall stoichiometry in excellent agreement with that

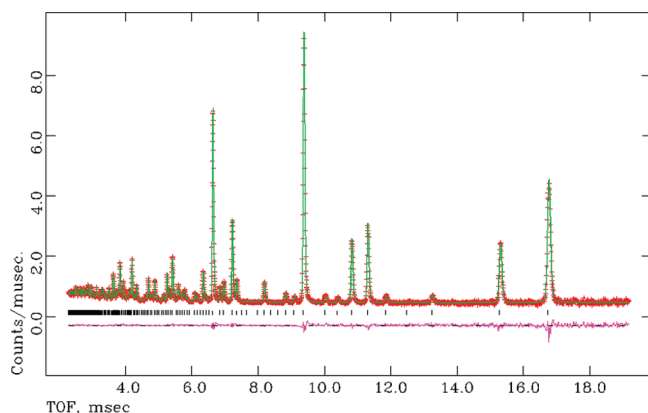


Figure 9. Observed, calculated, and difference profiles from ToF ND data for $\text{Li}_2\text{ZnGe}_3\text{O}_8$ at room temperature.

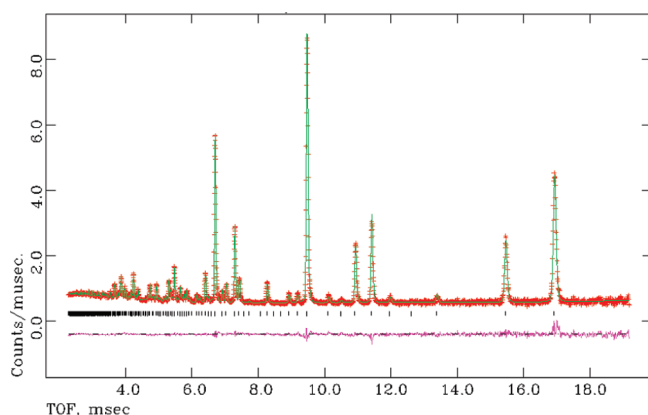


Figure 10. Observed, calculated, and difference profiles from ToF ND data for $\text{Li}_2\text{ZnGe}_3\text{O}_8$ at 850 °C, using a model with Li distributed over four crystallographic sites (Table 4).

expected. It must, however, be emphasized that the suggestion of Li for a 24e site is tentative; the refined occupancy for this site is only 0.041 (8), which, while statistically significant, represents a very small degree of scattering.

Interatomic $\text{Li}_{4b}\text{--Li}_{4a}$ distances (2.930 Å) are significantly longer in $\text{Li}_2\text{ZnGe}_3\text{O}_8$ than $\text{Li}_{8c}\text{--Li}_{12d}$ distances in $\text{Li}_2\text{NiGe}_3\text{O}_8$. $\text{Li}_{4b}\text{--Li}_{24e}$ and $\text{Li}_{24e}\text{--Li}_{4a}$ distances are 2.081 and 1.566 Å, respectively.

DISCUSSION

Li^+ -Ion Conduction Mechanisms in Complex Lithium Spinel. Conductivity, σ , is in general given by the equation $\sigma = ne\mu$, where n is the number of carriers of charge e and mobility μ . As the temperature increases, μ generally increases; i.e., it is more likely that a cation will have sufficient energy to hop from its ideal position into a vacant site. Oxygen atoms also vibrate more, oscillating around from their ideal positions and widening the bottlenecks in polyhedral faces, further facilitating ionic movement. Variable-temperature neutron powder diffraction experiments allow the capture of a time- and spatially-averaged snapshot of a crystal structure, with a distribution of mobile cations over the crystallographic sites occupied during data collection.

Table 4. Refined Structure Parameters and Derived Bond Lengths for $\text{Li}_2\text{ZnGe}_3\text{O}_8$ at 850 °C

space group	$P4_332$
a (Å)	8.28823 (17)
V (Å ³)	569.358 (35)
χ^2	2.070
R_{wp} (%)	2.52
R_{p} (%)	3.83
refined stoichiometry	$\text{Li}_{2.00(2)}\text{ZnGe}_3\text{O}_8$
cation site 8c	
x ($= y = z$)	0.00492 (56)
site occupancy	0.5 Li/0.5 Zn
U_{iso} (Å ²)	0.0108 (7)
cation site 4b	
x ($= y = z$)	0.625
site occupancy	0.618 (21) Li
U_{iso} (Å ²)	0.005
cation site 4a	
x ($= y = z$)	0.125
site occupancy	0.132 (17) Li
U_{iso} (Å ²)	0.005
cation site 24e	
x	0.9847 (109)
y	0.1801 (71)
z	0.0110 (105)
site occupancy	0.041 (8) Li
U_{iso} (Å ²)	0.005
cation site 12d	
x	0.125
y	0.37623 (13)
z	0.87378 (13)
site occupancy	1.0 Ge
U_{iso} (Å ²)	0.0104 (2)
oxygen site 1, O1, 8c	
x ($= y = z$)	0.38738 (17)
site occupancy	1.0 O
U_{iso} (Å ²)	0.0142 (5)
oxygen site 2, O2, 24e	
x	0.09689 (14)
y	0.13340 (17)
z	0.39420 (16)
site occupancy	1.0 O
U_{iso} (Å ²)	0.0134 (2)
bond length (Å)	
$\text{Li}/\text{Zn}_{8c}\text{--O1}$	2.043 (8) \times 1
$\text{Li}/\text{Zn}_{8c}\text{--O2}$	1.9731 (23) \times 3
$\text{Li}_{4b}\text{--O2}$	2.1602 (14) \times 6
$\text{Li}_{4a}\text{--O2}$	2.2444 (12) \times 6
$\text{Li}_{24e}\text{--O2}$	2.27 (8) \times 1, 2.33 (7) \times 1, 1.70 (8) \times 1, 1.68 (8) \times 1
Ge--O1	1.9652 (19) \times 2
Ge--O2	1.8565 (18) \times 2, 1.9268 (13) \times 2

Our results show Li diffuses through $\text{Li}_2\text{NiGe}_3\text{O}_8$ via a simple hopping mechanism. Li normally resides in tetrahedral 8c sites and occasionally migrates to one of three neighboring vacant 12d octahedral sites with which it shares a common edge, traveling via

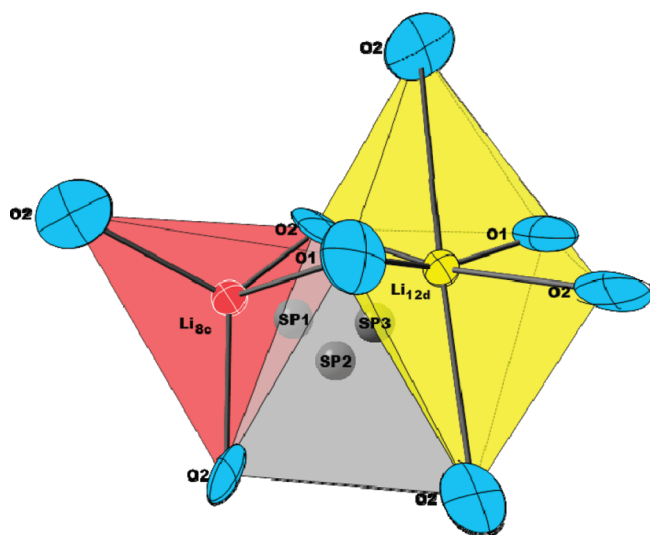


Figure 11. Portion of the $\text{Li}_2\text{NiGe}_3\text{O}_8$ crystal structure, showing a (red) $\text{Li}_{8c}\text{-O}_4$ tetrahedron and a nearest neighbor (yellow) $\text{Li}_{12d}\text{-O}_6$ octahedron. Three possible saddle points in the conduction pathway, the tetrahedral and octahedral faces and the empty tetrahedral site, are colored gray. For the sake of clarity, NiO_6 and GeO_6 octahedra were omitted.

the bottlenecks of one tetrahedral face bounded by O1 and two O2 anions, a vacant $\square\text{O}_4$ tetrahedral site, and then the octahedral face (Figure 11). Once on the 12d site, the migrating Li cation can move to the next nearby 8c site, or back from whence it came, resulting in a three-dimensional 8c–12d–8c zigzag conduction network. There is no evidence in our data of any other intermediate sites in the hopping process; refinement of either position or occupancy for a third Li site around the centroid position of the vacant $\square\text{O}_4$ tetrahedron did not converge to a stable value, and difference Fourier maps did not suggest the presence of an occupied site here, indicating that the vacant tetrahedral site is simply a saddle point in the conduction pathway, without any significant residence time.

Other saddle points in the 8c–12d pathway are the centers of the 8c tetrahedral and 12d octahedral faces. Analyses of the distances between these points and the bounding oxygen anions (Table 5) show that these windows are rather small, especially considering the Shannon effective ionic radii²⁷ for tetrahedrally coordinated Li cations of 0.59 Å. For example, simple geometrical calculations indicate a radius of ~ 0.55 Å for the tetrahedral window; these bottlenecks in the polyhedral faces must represent a significant barrier to Li diffusion. Ishizawa et al.¹⁴ previously commented on the role that the harmonic oscillations of oxygen atoms around their ideal positions must play in opening this bottleneck for ion hopping to occur. The shape of the anisotropic thermal ellipsoids for O1 and O2 shows some evidence of the displacement of oxygens away from their ideal positions in $\text{Li}_2\text{NiGe}_3\text{O}_8$, which likely plays a similar role in Li-ion conduction.

$\text{Li}_2\text{ZnGe}_3\text{O}_8$ was shown by Kawai et al. to be a very poor Li-ion conductor.²⁴ Zn partially occupies the 8c site, thereby partially blocking any 8c–12d–8c conduction pathway; there was no evidence in our data of any Li on a 12d site or Li on the 8c site being involved in conduction. Instead, it appears that Li migration involves a more tortuous and lengthier path. As the 4b– O_6 and 4a– O_6 octahedra are edge-sharing, direct 4b–4a migration is not plausible; instead, Li ions must hop from the 4b site,

Table 5. Saddle Point–Oxygen and –Lithium Distances (Å) of $\text{Li}_2\text{NiGe}_3\text{O}_8$ and $\text{Li}_2\text{ZnGe}_3\text{O}_8$ at 850 °C

$\text{Li}_2\text{NiGe}_3\text{O}_8$				
saddle point	O1	O2	Li_{8c}	Li_{12d}
SP1	1.828×1	1.889×2	0.807×1	1.691×1
SP2	1.757×1	1.800×1	1.441×1	1.490×1
		2.062×1		
		2.359×1		
SP3	1.463×1	2.284×1	1.718×1	0.981×1
		2.113×1		
$\text{Li}_2\text{ZnGe}_3\text{O}_8$				
saddle point	O2	Li_{4a}	Li_{4b}	
SP1	1.725×1	1.324×1	1.983×1	
	1.736×1			
	1.980×1			
Li_{24e}	$1.68(8) \times 1$	1.496×1	2.043×1	
	$1.70(8) \times 1$			
	$2.27(8) \times 1$			
	$2.33(7) \times 1$			
SP3	1.753×1	1.911×1	1.752×1	
	1.765×1			
	1.775×1			
	2.173×1			
SP4	1.676×1	2.141×1	1.162×1	
	1.727×1			
	2.017×1			

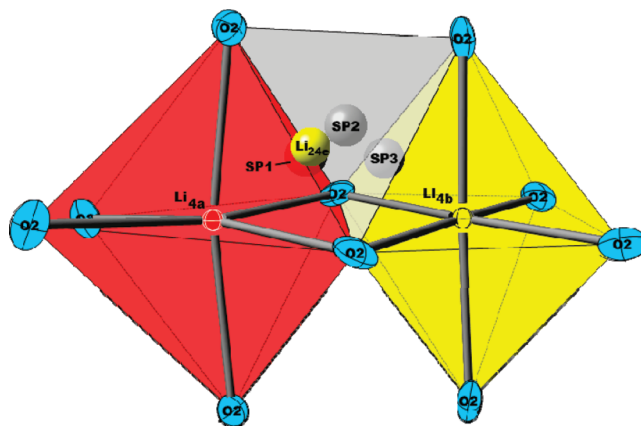


Figure 12. Portion of the $\text{Li}_2\text{ZnGe}_3\text{O}_8$ crystal structure, showing a (red) $\text{Li}_{4a}\text{-O}_6$ octahedron, a nearest neighbor (yellow) $\text{Li}_{4b}\text{-O}_6$ octahedron, and the (yellow) Li_{24e} site that may link them. $\text{Li}/\text{Zn}_{8c}\text{O}_4$ and GeO_6 polyhedra were omitted for the sake of clarity. Three possible saddle points in the conduction pathway and an empty tetrahedral site are colored gray.

through one of the octahedral faces in the direction of the 8c tetrahedra, and there is tentative evidence in our data of Li occupying a tetrahedrally coordinated 24e site along this conduction route, displaced from the centroid of the tetrahedron and closer to the saddle point in the tetrahedral face. Li can then hop

from the 24e site to the 4a site, resulting in a 4b–24e–4a–24e–4b conduction pathway (Figure 12). A comparison of possible saddle point-oxygen distances in this conduction pathway against those for $\text{Li}_2\text{NiGe}_3\text{O}_8$ (Table 5) shows that both tetrahedral and octahedral windows are smaller for $\text{Li}_2\text{ZnGe}_3\text{O}_8$. This, along with the reduced number of charge carriers, most likely explains the lower ionic conductivity and higher activation energy for conduction of $\text{Li}_2\text{ZnGe}_3\text{O}_8$ in comparison with $\text{Li}_2\text{NiGe}_3\text{O}_8$.

Increasing the size of either these polyhedral faces or intermediate sites may lead to materials with lower activation energies and higher ionic conductivities; doping the octahedral site(s) with larger or smaller cation(s) may influence the geometry of these obstacles. In the case of $\text{Li}_2\text{NiGe}_3\text{O}_8$, partial or complete replacement of Ge with either Ti or Si, respectively, may be considered. In addition, substitution of fluoride for oxygen has been shown²⁸ to increase the size of the bottleneck in lithium lanthanum titanate perovskites, reducing the activation energy required for ion migration; replacement of O with F could similarly be attempted for complex lithium spinels. Such approaches may also prove to be important in the development of other materials with potential applications as solid electrolytes in Li-ion batteries.

CONCLUSIONS

Rietveld refinement of the crystal structures of $\text{Li}_2\text{NiGe}_3\text{O}_8$ and $\text{Li}_2\text{ZnGe}_3\text{O}_8$ has been conducted using variable-temperature time-of-flight neutron powder diffraction data. Conduction of Li ions through $\text{Li}_2\text{NiGe}_3\text{O}_8$ involves a simple 8c–12d–8c ion hopping mechanism. This may be facilitated by anisotropic displacements of oxygen atoms from their ideal positions, opening the bottleneck in the $\text{Li}_{8c}\text{–O}_4$ faces. The conduction mechanism in $\text{Li}_2\text{ZnGe}_3\text{O}_8$ appears to be more complex, involving a longer 4b–24e–4a–24e–4b pathway. The lower ionic conductivity of $\text{Li}_2\text{ZnGe}_3\text{O}_8$ can be explained by a reduction in the number of charge carriers and the smaller size of the appropriate polyhedral windows.

ASSOCIATED CONTENT

S Supporting Information. Crystallographic data files (CIF) for refinements and tables of crystal data, structure solution and refinement, atomic coordinates, bond lengths and angles, and (an)isotropic thermal parameters for $\text{Li}_2\text{NiGe}_3\text{O}_8$ and $\text{Li}_2\text{ZnGe}_3\text{O}_8$ at 850 °C refined using the initial structural model. This material is available free of charge via the Internet at <http://pubs.acs.org>.

ACKNOWLEDGMENT

We thank EPSRC for funding and Alejandro Várez for useful discussions. Neutron scattering beamtime was provided by the Science and Technology Facilities Council.

REFERENCES

- (1) Park, M.; Zhang, X.; Chung, M.; Less, G. B.; Sastry, A. M. *J. Power Sources* **2010**, *195* (24), 7904–7929.
- (2) Kawai, H.; Nagata, M.; Tukamoto, H.; West, A. R. *Electrochem. Solid-State Lett.* **1998**, *1* (5), 212–214.
- (3) Belous, A. G.; Novitskaya, G. N.; Polyanskaya, S. V.; Gornikov, Y. I. *Zh. Neorg. Khim.* **1987**, *32* (2), 283–286.

- (4) Inaguma, Y.; Chen, L.; Itoh, M.; Nakamura, T.; Uchida, T.; Ikuta, M.; Wakihara, M. *Solid State Commun.* **1993**, *86*, 689.
- (5) Itoh, M.; Inaguma, Y.; Jung, W.; Chen, L.; Nakamura, T. *Solid State Ionics* **1994**, *70/71*, 203.
- (6) Cussen, E. J. *Chem. Commun.* **2006**, *4*, 412–413.
- (7) Thangadurai, V.; Kaack, H.; Weppner, W. J. F. *J. Am. Ceram. Soc.* **2003**, *86* (3), 437–440.
- (8) Thangadurai, V.; Schwenzel, J.; Weppner, W. *Ionics* **2005**, *11*, 11–23.
- (9) Ramzy, A.; Thangadurai, V. *ACS Appl. Mater. Interfaces* **2010**, *2* (2), 385–390.
- (10) Geiger, C. A.; Alekseev, E.; Lazic, B.; Fisch, M.; Armbruster, T.; Langner, R.; Fechtelkord, M.; Kim, N.; Pettke, T.; Weppner, W. *Inorg. Chem.* **2011**, *50* (3), 1089–1097.
- (11) Thangadurai, V.; Weppner, W. *Ionics* **2006**, *12* (1), 81–92.
- (12) Várez, A.; Inaguma, Y.; Fernández-Díaz, M. T.; Alonso, J. A.; Sanz, J. *Chem. Mater.* **2003**, *15* (24), 4637–4641.
- (13) Yashima, M. *J. Ceram. Soc. Jpn.* **2009**, *117* (10), 1055–1059.
- (14) Ishizawa, N.; du Boulay, D.; Hayatsu, M.; Kuze, S.; Matsushima, Y.; Ikuta, M.; Wakihara, M.; Tabira, Y.; Hester, J. R. *J. Solid State Chem.* **2003**, *174*, 167–174.
- (15) Ishizawa, N.; Tateishi, K. *J. Ceram. Soc. Jpn.* **2009**, *117* (1), 6–14.
- (16) Laumann, A.; Boysen, H.; Bremholm, M.; Fehr, K. T.; Hoelzel, M.; Holzapfel, M. *Chem. Mater.* **2011**, *23*, 2753–2759.
- (17) Bragg, W. H. *Philos. Mag.* **1915**, *30* (176), 305–315.
- (18) Nishikawa, S. *Proc. Math. Phys. Soc. Tokyo* **1915**, *8*, 199–209.
- (19) Sickafus, K. E.; Wills, J. M.; Grimes, N. W. *J. Am. Ceram. Soc.* **1999**, *82* (12), 3279–3292.
- (20) Durif, A.; Joubert, J. C. R. *Acad. Sci. Paris* **1962**, *255*, 2471.
- (21) Blasse, G. *J. Inorg. Nucl. Chem.* **1963**, *25* (6), 743–744.
- (22) Reeves, N.; Pasero, D.; West, A. R. *J. Solid State Chem.* **2007**, *180* (6), 1894–1901.
- (23) Powder Diffraction File Card No. 48-260.
- (24) Kawai, H.; Tabuchi, M.; Nagata, M.; Tukamoto, H.; West, A. R. *J. Mater. Chem.* **1998**, *8* (5), 1273–1280.
- (25) Toby, B. H. *J. Appl. Crystallogr.* **2001**, *34*, 210–213.
- (26) Larson, A. C.; Von Dreele, R. B. *Los Alamos Natl. Lab., [Rep.] LA (U.S.)* **2000**, 86–748.
- (27) Shannon, R. D. *Acta Crystallogr.* **1976**, *A32*, 751–767.
- (28) Okumura, T.; Ina, T.; Orikasa, Y.; Arai, H.; Uchimoto, Y.; Ogumi, Z. *J. Mater. Chem.* **2011**, *21*, 10061–10068.